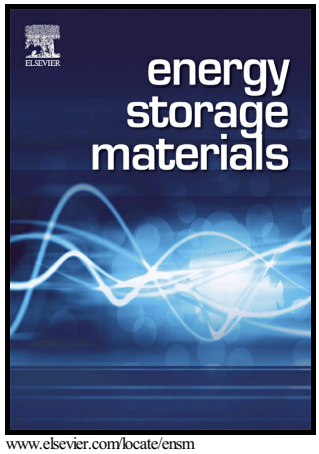

www.elsevier.com/locate/ensm

A Textile-Based SnO_2 Ultra-Flexible Electrode for Lithium-Ion Batteries

Xin Min, Bin Sun, Shi Chen, Minghao Fang, Xiaowen Wu, Yan'gai Liu, Amr Abdelkader, Zhaohui Huang, Tao Liu, Kai Xi, R. Vasant Kumar

PII: S2405-8297(18)30709-8
DOI: https://doi.org/10.1016/j.ensm.2018.08.002
Reference: ENSM469

To appear in: *Energy Storage Materials*

Received date: 4 June 2018
Revised date: 29 July 2018
Accepted date: 2 August 2018

Cite this article as: Xin Min, Bin Sun, Shi Chen, Minghao Fang, Xiaowen Wu, Yan'gai Liu, Amr Abdelkader, Zhaohui Huang, Tao Liu, Kai Xi and R. Vasant Kumar, A Textile-Based SnO_2 Ultra-Flexible Electrode for Lithium-Ion Batteries, *Energy Storage Materials,* https://doi.org/10.1016/j.ensm.2018.08.002

A Textile-Based SnO_2 Ultra-Flexible Electrode for Lithium-Ion Batteries

Xin Min[a,b1*], Bin Sun[a1], Shi Chen[a], Minghao Fang[a], Xiaowen Wu[a], Yan'gai Liu[a], Amr Abdelkader[c], Zhaohui Huang[a], Tao Liu[d], Kai Xi[b,e*], R. Vasant Kumar[b]

[a]Beijing Key Laboratory of Materials Utilization of Nonmetallic Minerals and Solid Wastes, National Laboratory of Mineral Materials, School of Materials Science and Technology, China University of Geosciences (Beijing), Beijing, 100083, China

[b]Department of Materials Science and Metallurgy, University of Cambridge, Cambridge, CB3 0FS, United Kingdom

[c]Department of Design and Engineering, Faculty of Science & Technology, Bournemouth University, Poole, Dorset, BH12 5BB, United Kingdom

[d]Chemistry Department, University of Cambridge, Lensfield Road, Cambridge CB2 1EW, United Kingdom

[e]Cambridge Graphene Centre, Department of Engineering, University of Cambridge, Cambridge, CB3 0FA, United Kingdom

minx@cugb.edu.cn

kx210@cam.ac.uk

[*]Corresponding author.

[*]Corresponding authors at: Beijing Key Laboratory of Materials Utilization of Nonmetallic Minerals and Solid Wastes, National Laboratory of Mineral Materials, School of Materials Science and Technology, China University of Geosciences (Beijing), Beijing, 100083, China

[1] These authors contributed equally to this work.

Abstract

The advancements in wearable electronic devices make it urgent to develop high-performance flexible lithium-ion batteries (LIBs) with excellent mechanical and electrochemical properties. Herein, we design a new 3D hierarchical hybrid sandwich flexible structure by anchoring SnO_2 nanosheets (SnO_2-NSs) on flexible carbon cloth and coating with thin amorphous carbon (AC) layer (CF@SnO_2-NS@AC). The carbon cloth substrate works as the backbone and the current collector, while the thin AC layer provides extra support during the electrode expansion. The new architecture can be utilised as a binder-free electrode and presents extraordinary mechanical flexibility and outstanding electrical stability under external stresses. The new electrode can deliver a specific capacity as high as 968.6 mAh g^{-1} after 100 cycles at 85 mA g^{-1}, which also shows remarkable rate capability and an excellent high current cycling stability. The outstanding electrochemical performance combined with the high mechanical flexibility and invariable electrical conductivity during/after different bending cycles make the new structure a promising oxide anode for flexible batteries. With the possibility of using a similar approach to design flexible cathode, the present work opens the door to empower the next-generation wearable devices and smart clothes with a robust and reliable battery.

Graphical Abstract

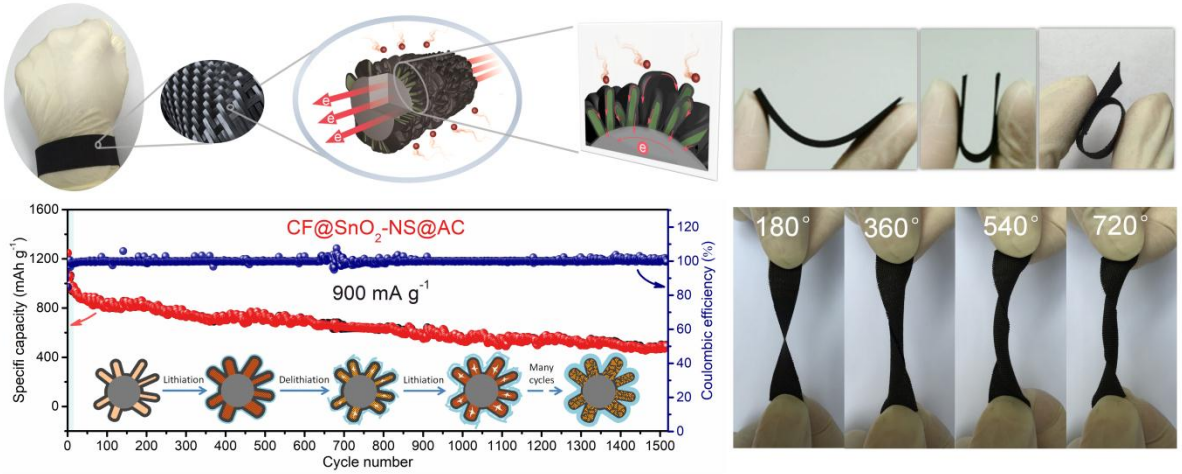

An ultra-flexible anode for lithium-ion batteries was developed using a novel 3D hierarchical sandwich structure. The novel anode used conductive textile as the backbone and the current collector and two-dimensional SnO_2 as the active materials. The electrode exhibits excellent mechanical flexibility and outstanding electrical stability under external stresses, in addition to the enhanced electrochemical performance. This electrode is a strong candidate to empower the next-generation wearable devices.

Keywords: Wearable devices; Flexible lithium-ion batteries; Tin dioxide; 3D hierarchical structure; Nanosheet; Textile anode.

1. Introduction

The rapid growth in wearable devices demands a new generation of energy storage devices that can fulfil the future design requirements.[1-5] Examples of these devices include wearable displays, military garment devices, sensors, high-performance sportswear, new mobile communication devices, and possibly even new classes of wearable computers.[6-9] To empower the new wearable devices, the energy storage system must have reasonable mechanical flexibility in addition to high energy and power density, good operational safety, long cycling life and the low cost.[2, 10, 11] Lithium-ion batteries (LIBs) are one of the most promising candidates to empower wearable devices because of the long cycle lifespan, high energy density, and high working voltage.[12-16] However, there are many challenges related to designing flexible LIBs suitable for wearable electronics. The electrodes of the conventional LIBs, typically made of brittle material powders such as graphite or oxides which are then coated on Cu or Al foil, which make them rigid and can easily delaminate, or crack, upon being subjected to mechanical strain.[17-20]

Many approaches have been explored to design fully flexible LIBs electrodes. One typical approach is improving the adhesion between the active materials and the metallic current collector by adding fluorine-based polymer binder.[21-23] However, the improvement in the mechanical stability comes at the expense of the energy density. The addition of insulating binder increases the electrochemical impedance, forms a thin adhesion between the active layers and the current collector substrate, which weakens the cohesion among the composition of the electrode components.[23-25] The binder also has a negative effect on the volumetric capacity since it introduces electrochemically inert materials into the overall volume of the electrode.[26, 27] Another approach for improving the flexibility of the LIBs electrodes is by reinforcing them with conductive 1D or 2D materials.[28-30] Additives such as carbon nanotubes[8], cellulose nanofibers[31], graphene[32], and microfiber[33] have

been reported to enhance the mechanical stability of the electrodes under strain. However, it is still a challenge to meet the flexibility requirements of many wearable electronics with the simple physical mixing due to the poor contact between the active materials and the reinforcing materials.[26, 33] In addition, the reinforcing agents are usually electrochemically passive, which reduces the volumetric capacitance.[16, 33, 34] Growing the active materials directly on a flexible network provides a strong interaction and leads to robust electrodes without scarifying the energy density.[29, 33, 35] These flexible substrates include both conductive and nonconductive materials, such as metal mesh, carbon cloth, free-standing films of carbon materials, and the insulating polyethylene terephthalate films.[34-41]

Despite the several attempts, there is still a huge gap between the reported technologies and the targeted specification, particularly regarding flexibility and electrochemical stability. Also, engineering high-performance flexible energy storage devices through a cost-effective and scalable method remains a challenge. Another important challenge that is shared between flexible and nonflexible LIBs is the limited specific capacity of the conventional graphite anode (372 mAh g^{-1}).[42, 43] Transition metal oxides have attracted much attention and are rendered as the promising anodes for the next-generation LIBs due to their high theoretical capacity, abundance and low-cost.[44-47] Amongst them, tin dioxide (SnO_2) has a theoretical specific capacity of 781 mAh g^{-1} as a result of the reversible alloying/dealloying process between Sn and Li.[48-52] However, the poor electric conductivity of SnO_2 limits the rate capability and the cycle life of the electrodes.[53, 54] Also, the drastic volume change during the alloying/dealloying cycles causes serious structural disintegration problems within the anode and subsequently a quick capacity fading.[55, 56] Moreover, transition metal oxides are more mechanically rigid than graphite and are difficult to be used directly for the highly flexible LIBs.[16, 57, 58] One effective route to address the challenges of the poor cycle life and capacity fading is by reducing the dimensions of the SnO_2 particles to accommodate the

volumetric changes. Recently, electrodes based on SnO_2 nanoparticles[59, 60], nanowires[61, 62], nanosheets[63, 64], nanotubes[65, 66], porous nanoflakes[67, 68], or hollow nanostructure[69, 70] have been tested. Arranging the nanomaterials into 3D architectures has also been investigated.[71, 72] In addition, electrodes based on core-shell structures[73, 74], 3D hierarchical porous architectures[75, 76], and sandwich structures[77, 78], associated with good mechanical stability, large surface area, and numerous active sites receive wide exploitation in supercapacitors and batteries.[79-81] However, most of these new 3D structural tin dioxide materials are not suitable for flexible devices either because they have poor electrical conductivity, or because they require expensive methods for preparation. It is, therefore, necessary to develop new flexible oxide electrodes that can meet the energy and the mechanical flexibility requirements by combining both the flexible design approaches and 3D hierarchical architectures into one-electrode configurations.

In this work, we demonstrate a novel 3D hierarchical hybrid sandwich flexible structure, which was developed by coating thin amorphous carbon (AC) layer on a free-standing ultrathin SnO_2 nanosheets (SnO_2-NSs) film anchored on carbon fiber (CF) textile substrate (Fig. 1a). The three-layered structure, designated as CF@SnO_2-NS@AC, was used to fabricate the electrodes without the addition of any binder. The new structure presents multiple advantages as a flexible anode for LIBs, as shown in Fig. 1b. First, the SnO_2 nanosheets are chemically bonded to the conductive carbon cloth offering a robust adhesion between the active materials and the substrate. Second, the free-standing ultrathin SnO_2 nanosheets are interlinked to form a 3D self-supported network, which enhances the structural stability and also facilitates the electrolyte diffusion within the electrode. The porosity of the active materials helps accommodate the volumetric changes during the alloying/dealloying process. In addition, the amorphous carbon layer coating provides extra structural protection and also prevents the agglomeration of the active materials during the

electrochemical reactions. Moreover, the unique sandwiched flexible structure and superior chemical reinforcement can ensure the flexibility, strength, and dimensional stability of the electrodes during repeated extreme deformation caused by bending, folding, rolling or twisting. The 3D hierarchical CF@SnO_2-NS@AC flexible architectures show a high discharge specific capacity of about 968.5 mAh g^{-1} after 100 cycles at a current density of 85 mA g^{-1}, which is about 96% reversible discharge capacity retention of the 10th cycles. The electrode has an excellent rate capability judged by the stable discharge capacity of about 656.2 mAh g^{-1} cycled at a current density as high as 1500 mA g^{-1}. In addition, the CF@SnO_2-NS@AC composite also presents a high discharge capacity of 471.2 mAh g^{-1} after 1500 cycles at a high current density of 900 mA g^{-1}.

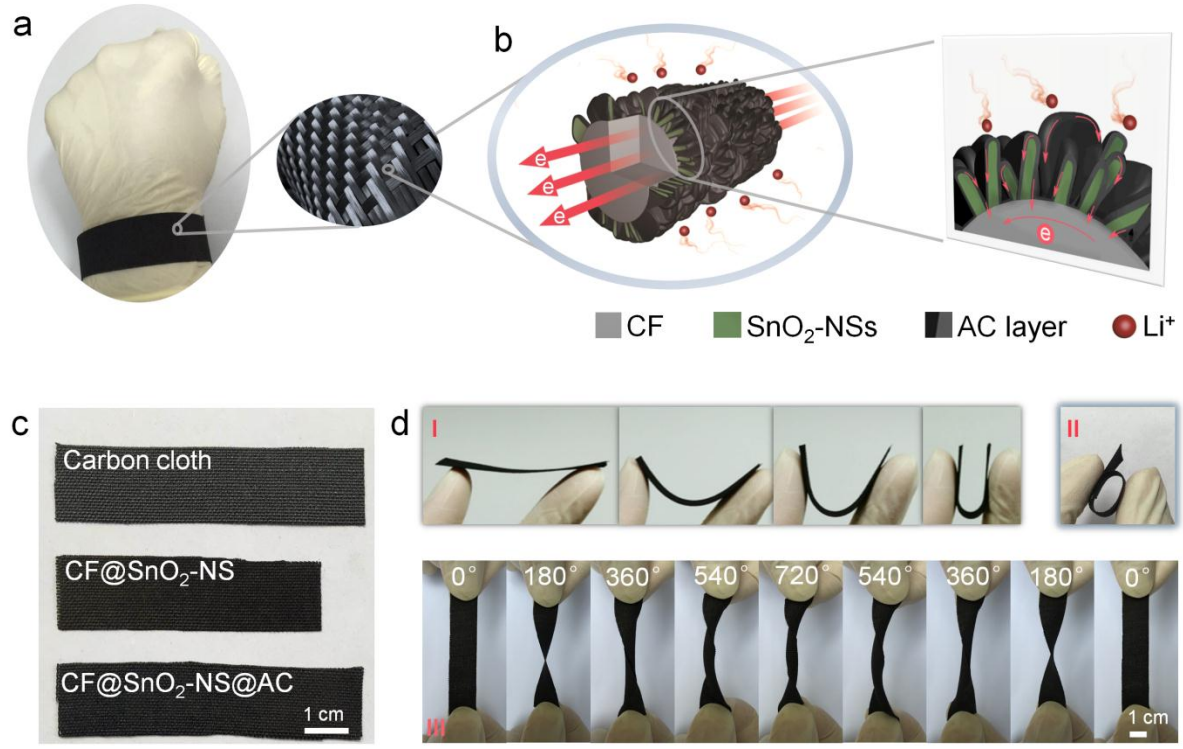

Fig. 1. Schematic illustration for the structural features (a, b) of the 3D hierarchical CF@SnO_2-NS@AC sandwich structure on the wearable carbon cloth, digital photographs (c) of the as-prepared products and the photos (d) of the flexible CF@SnO_2-NS@AC electrode during the folding (I), the rolling (II), and twisting (III) tests.

2. Results and discussion

The multi-step growth processes for the 3D hierarchical CF@SnO_2-NS@AC and CF@SnO_2-NP@AC flexible electrodes are illustrated in Fig. 2a and Fig. S1. The wearable carbon cloth, composed of CF yarn, was chosen as the substrate material because of its well-known flexibility and conductivity. Firstly, the SnO_2-NSs and SnO_2-NPs were grown on the surface of the CF to yield the hierarchical CF@SnO_2-NS and CF@SnO_2-NP structures by a hydrothermal method followed by a heat treatment step in the air. In the second step, both CF@SnO_2-NS and CF@SnO_2-NP were coated with a layer of AC through another hydrothermal and a subsequent annealing process.

The digital photographs of the carbon cloth, the resultant 3D self-supported CF@SnO_2-NS structure, and the sandwiched CF@SnO_2-NS@AC flexible composites are shown in Fig. 1c. The color of the carbon cloth became darker after the hydrothermal and annealing treatment, which implies that the SnO_2-NS layer and AC layer were successfully coated on the CF substrate. The optical image in Fig. 1d(I-III) display the excellent flexibility and the well-woven structure of the CF@SnO_2-NS@AC electrodes. No apparent changes were observed on the CF@SnO_2-NS@AC electrode during the bending, twisting, folding, crumpling or the rolling tests. Furthermore, the mechanical adhesion between the active materials and the current collector was determined by the standard tape test. No visible particles or flake delamination could be observed on the tape. The electrode was also subjected to test under a stream of water, and no apparent contamination was observed in the water stream, which proved the strong adhesion between the electrode components NS@AC.

We have investigated the morphology of the new electrodes using the field emission scanning electron microscopy (FESEM), the transmission electron microscopy (TEM), and the high-resolution TEM (HRTEM). The corresponding images are shown in Fig. 2b-h. The structure of the carbon cloth is presented in Fig. S2, which shows that the CFs have smooth

surfaces and an average diameter of about 9 μm. Fig. S3a-c shows the morphology of the CF@SnO_2-NS structure after the hydrothermal reaction, which indicates that the SnO_2-NSs are successfully grown and uniformly distributed on the CF substrate without any aggregations. The SnO_2-NSs are interlinked to form a self-supported sponge-like architecture that is anchored on the conductive CF. Heating the sample in the air did not cause any structural damage as can be seen in Fig. 2b, c. However, the HRTEM image after the first heat treatment (Fig. 2d) shows distinguished lines for the atomic in-plan arrangements, suggesting that the SnO_2-NSs are of good crystallinity. The marked interplanar distance of the horizontal lines is about 0.343 nm, corresponding to the (110) crystal planes of the SnO_2-NSs, while the interplanar distance of around 0.268 nm for the vertical lines belongs to the (101) crystal planes, confirming that the SnO_2 nanostructures grow predominantly along the (101) crystal planes direction. The selected-area electron diffraction (SAED) pattern (Fig. S4) shows intermittent diffraction rings and bright diffraction points, further confirming the crystallinity of the SnO_2-NSs after heat treatment. The EDS analysis (Fig. S5) reveals that the self-supported composites are mainly composed of C, Sn, and O elements. In order to confirm the 2D nature of the SnO_2-NSs, we have isolated the SnO_2 flakes from the composites, using sonication. Strong and prolonged sonication was needed to peel off the flakes and to break the strong bond with the CF. The TEM images of the isolated SnO_2 products indicate a plate-like structure (Fig. S6a, b). The average size of the isolated flakes is about 50 nm, which is almost one quarter of that of the as-synthesized flakes. The massive reduction of the size during the sonication signifies the excessive energy required to break the bond between CF and SnO_2-NSs. By comparing the HRTEM and the SEM images, the thickness of the SnO_2-NSs is calculated to be about 4-6 nm.

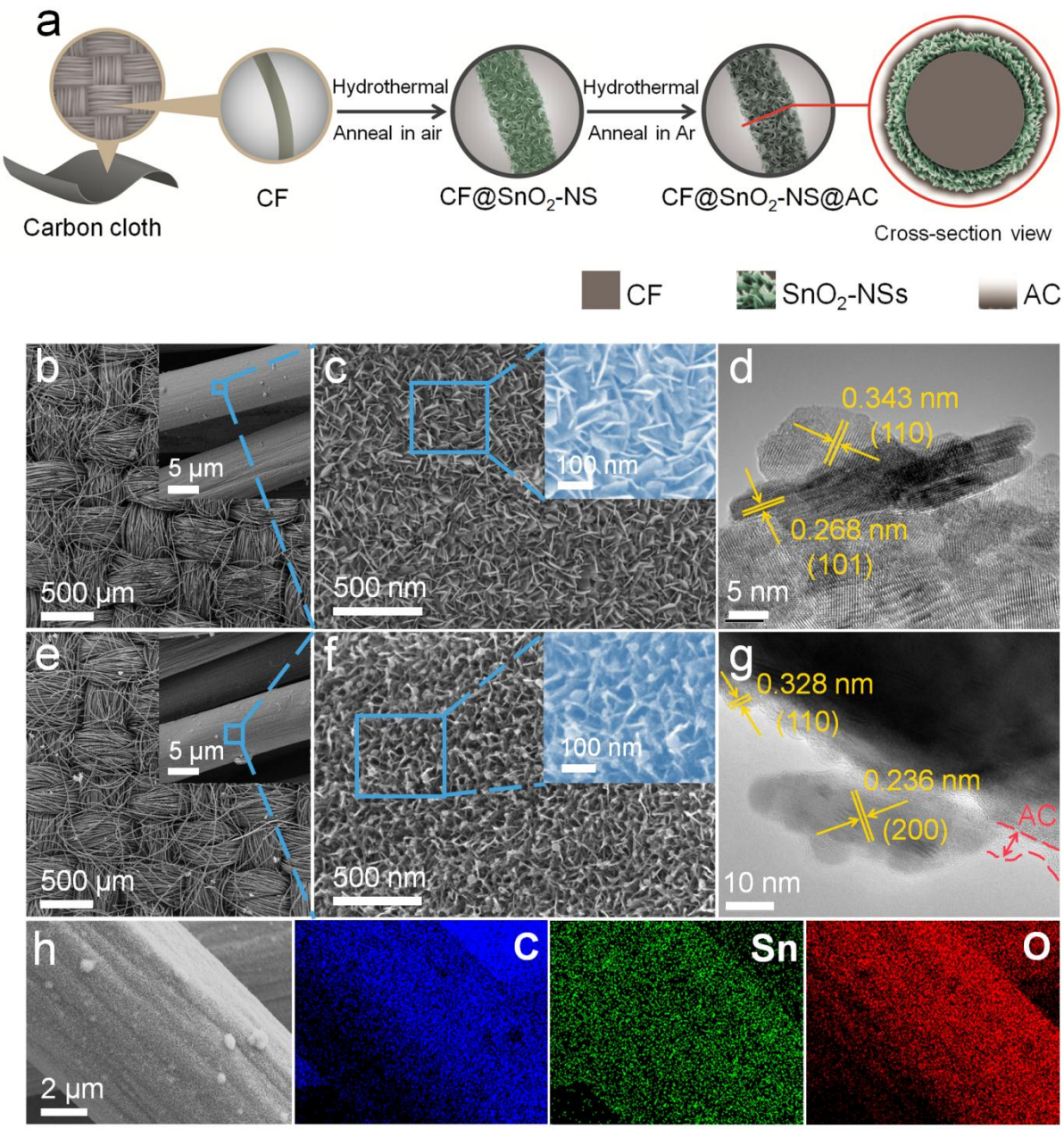

Fig. 2. (a) Formation scheme of the 3D hierarchical flexible composites CF@SnO_2-NS@AC. (b, c) FSEEM and (d) HRTEM images of the CF@SnO_2-NS composite after thermal treated at 500 °C for 3h in the air. (e, f) FESEM, (g) HRTEM images, and (h) EDS mapping of the CF@SnO_2-NS@AC sample. The inset images show the high-resolution SEM morphologies of CF@SnO_2-NS (b, c) and CF@SnO_2-NS@AC (e, f), respectively.

The final step in preparing the multilayer electrode was to coat the CF@SnO_2-NS with a thin layer of AC via a facile hydrothermal method followed by annealing at 500 °C in an Ar atmosphere. The FESEM images of the composite after coating (Fig. 2e, f and Fig. S7) shows no change in the morphology of the SnO_2-NSs on both of the two sides of the products. The

inset images of Fig. 2b, e show that the carbon cloths have kept their woven structure and therefore the hierarchical structure of the electrode has also been maintained. The EDS elemental mappings (Fig. 2h) confirmed that all the elements detected prior to the AC coating were still homogeneously distributed across the electrode. The diameter of the CF increased by about 0.5 μm after being coated with SnO_2-NSs, and the change after AC coating was negligible. The TEM and HRTEM images in Fig. 2g and Fig. S6c, d reveal the core-shell structure of the SnO_2-NS@AC with the thickness of the AC layer about 2-4 nm. The interplanar lines of the SnO_2 are hardly visible in the HRTEM image (Fig. 2g) due to the full coverage with the amorphous AC layer. The interplanar distance on the top left corner is about 0.328 nm, which represents the (110) crystal plane spacing of the SnO_2-NSs. The marked interplanar distance in the central area exhibiting the microstructure of SnO_2 from the side is measured to be about 0.236 nm, which corresponds to the (200) planes. X-ray diffraction (XRD) was also used to further investigate the crystallographic structure and the phase purity of the CF@SnO_2-NS@AC electrode. The XRD pattern of the final electrode materials is illustrated in Fig. 3a. The broad peak at 26° and the implicit peak at 44° are features of amorphous carbon of the carbon cloth substrates and the coated AC layer. All other diffraction peaks can be indexed to the tetragonal SnO_2 crystalline structures (Pdf No. 88-287), which strongly confirms the high purity of CF@SnO_2-NS@AC. The crystallinity of the carbon substrate and the AC layer was further investigated with Raman spectroscopy. Overall, there are two first-order Raman bands; namely, the D band centred at ~ 1350 cm^{-1} and the G band at ~ 1590 cm^{-1}.[82] The intensity ratio between the D and G bands I_D/I_G has been widely used as a semi-quantitative method to determine the structural order or the crystallite size of the carbon materials.[83] It is clear from Fig. 3b that the ratio I_D/I_G decreases after coating the CF with both SnO_2-NSs and AC due to the amorphous nature of

the AC layer.[84-86] Also, the position of the G band has shifted to the left and the separation between the two bands has almost vanished after the AC coating.[87, 88]

To further gain insights into the growth mechanism of the SnO_2-NSs on the carbon cloth substrate, the hydrothermal process products at different reaction time were studied by FESEM (Fig. S8). At the first stage of the process, SnO_2 nanoparticles grow slowly on the surface defects of CF and result in a rougher surface compared with the pure CF (Fig. S8a). Then these SnO_2 nanoparticles serve as a nucleus for the further growth, and some tiny SnO_2-NSs begin to form in a direction perpendicular to the CF surface. The SnO_2-NSs fully cover the substrates within the first few hours of the process (Fig. S8b). The tiny SnO_2-NSs then gradually grow in size until the integrated SnO_2-NSs porous layer is formed (Fig. S8c). As the reaction continues, some new SnO_2-NSs grow on the top of the SnO_2-NSs layer. The SnO_2-NSs are interconnected at the edges and corners, which finally lead to the honeycomb-like porous structure (Fig. S8d). Increasing the reaction time for more than 12 hours causes the unwanted aggregation of SnO_2-NS to form solid clusters. These clusters are not connected directly to the conductive substrate and are poorly connected to the older SnO_2-NSs. As a result, many of these late-formed clusters are readily removed by water during the washing step. However, all grown SnO_2-NSs at different treatment times have almost the same thickness. Therefore, we select 12 hours to be the optimal time for the hydrothermal process. The growth mechanism is schematically illustrated in Fig. S8e. By the way, the ratios of raw materials including stannous chloride and glucose were optimized as shown in Fig. S9 and Fig. S10. The phase purity and morphology of the CF@SnO_2-NP@AC composite were also investigated in Fig. S11 and Fig. S12.

The adhesion between the active materials and the current collector plays a crucial role in the life of the electrode and its ability to resist mechanical damage. One important aim of the present work is to create a chemical bond between the active materials (SnO_2-NSs) and the

carbon cloth substrate that serves as the current collector. Therefore, we have conducted XPS analysis to investigate the type of bonding between the different components of the CF@SnO_2-NS@AC electrode. The results of the XPS analysis are shown in Fig. 3d-f and Fig. S13. The survey spectrum in Fig. S13 indicated the presence of the typical signals of elements Sn (3s, 3p, 3d, 4s, 4p, 4d), O (1s), and C (1s), in agreement with the EDS analysis. The high-resolution C 1s spectrum can be split into three distinguished peaks corresponding to the C=C bond and some other different oxygen-containing functional groups such as C-O and C=O bonds (Fig. 3d).[89] The symmetric XPS peaks centred at 487.3 and 495.7 eV can be ascribed to Sn-O $3d_{5/2}$ and Sn-O $3d_{3/2}$ bonding of SnO_2 respectively (Fig. 3e).[56, 89] Furthermore, the O 1s spectrum in Fig. 3f consists of three peaks at 531.4, 532.4, and 533.4 eV attributing to the O-Sn bond, Sn-O-C bond, and the O 1s in O_2, confirming that the SnO_2-NSs is chemically bonded to CF and AC. The mass fraction of SnO_2-NSs in the as-prepared samples was determined by the thermogravimetric analysis (TGA, Fig. S14). Both composites showed significant mass loss between 650 and 850 °C owing to the combustion of CF and AC. The SnO_2-NSs loading on the CF is estimated to be about 20%, which gives a surface loading of 3.2 mg/cm^2 as stated in the *Experiment Section* (see *ESI*).

As the electrochemical performance of electrodes depends on the specific surface area of the CF@SnO_2-NS@AC, it was evaluated by N_2 adsorption/desorption isotherms (the resulted isotherm measured at 70 K is illustrated in Fig. S15). As shown in Fig. 3c, the specific surface area of the carbon cloth substrate was estimated to be 7.86 m^2/g, increased to 17.86 m^2/g and 20.95 m^2/g after being coated with SnO_2-NSs and AC, respectively. In contrast, the BET specific surfaces (Fig. S16) of the CF@SnO_2-NP (7.88 m^2/g) and CF@SnO_2-NP@AC (17.42 m^2/g) are much lower than that of the SnO_2-NSs-based samples, which is in excellent agreement with the SEM images in Fig. S12. Consequently, all the characterization results indicate that the CF@SnO_2-NS@AC composites feature a 3D sandwich hierarchical porosity

structure with a high surface area, which allows for stable structural integrity, fast ion transport and electron transfer rates without any additives for high-performance LIBs applications.

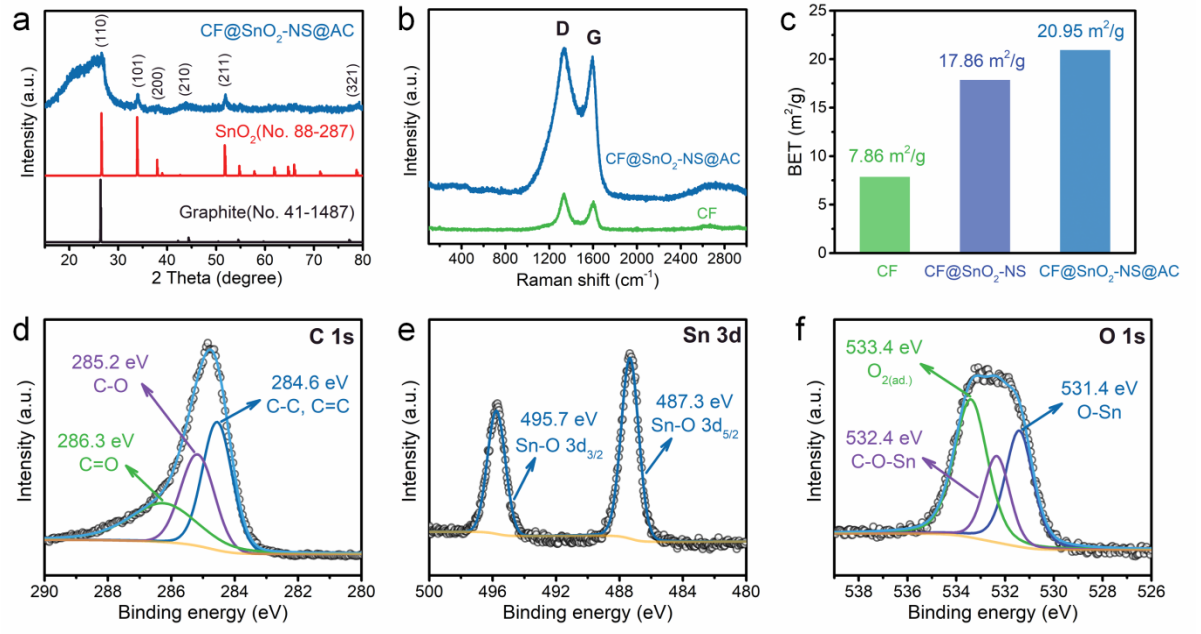

Fig. 3. XRD (a), Raman spectra (b), and BET specific surface area (c), XPS high-resolution spectra of C 1s (d), Sn 3d (e), and O 1s (f) of the as-prepared CF@SnO_2-NS@AC sample.

We have first examined the electric stability of the CF@SnO_2-NS@AC at different bending and folding degrees (Fig. 4a and Fig. S17). Fig. 4b shows the recorded current-potential (I-V) curves of the electrode after different repeated bending cycles, of which each cycle is shown in Fig. S16. It can be seen that the CF@SnO_2-NS@AC presents a superior electrical conductivity and there is no apparent performance change in the electrochemical response after 200 bending cycles, indicating excellent electric stability for the 3D hierarchical structure. Furthermore, the current response upon applying a constant voltage shows negligible changes at different bending angles. Fig. 4c shows that the current is stable at about 17.3 mA during all the bending stages of the first cycle. After 200 repeated bending cycles, the value of current is 16.8 mA, and no apparent changes can be observed under bending. The SEM images (Fig. S18) also confirm that the CF@SnO_2-NS@AC electrodes

can maintain superior structural integrity even after 200 bending cycles and ultrasonic treatment for 15 mins and after the twisting test shown in Fig. 1d.

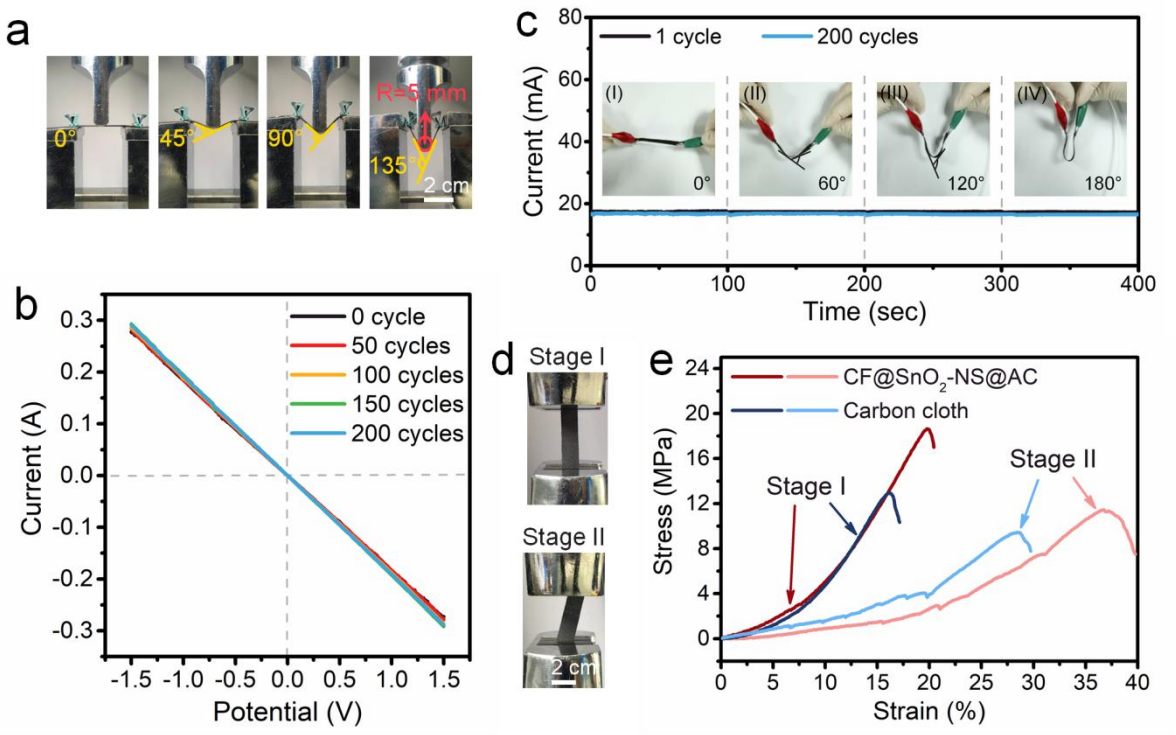

Fig. 4. (a) Illustration of bending the prepared CF@SnO_2-NS@AC flexible composites at different angles in one cycle according to the 3-point bending test setup, (b) current-potential curves of the as-prepared CF@SnO_2-NS@AC flexible composites after different repeated bending cycles, (c) current-time curves of the composite samples at various bending angles of the 1st and 200th cycles, and the inset images show the corresponding bending angles for measurement, photographs (d) of the tensile strength test on the carbon cloth at stages I and II, and the stress-strain curves (e) of CF@SnO_2-NS@AC and carbon cloth substrate.

Moreover, the dynamic mechanical analysis in different directions (Fig. 4d) was examined by the tensile strength testing. The stress-strain curve in Fig. 4e shows that the mechanical properties of the CF@SnO_2-NS@AC composites display insignificant variations in various directions arising possibly from their braided structure. A more considerable tensile strength at Stage I is maintained about 18.6 MPa with an excellent elongation of 19.7%, and a smaller tensile strength at Stage II is about 11.5 MPa with 36.8% strain, which indicates an excellent strength and elastic deformation capability. The values of both tensile strengths and elongations in all directions are much larger than those of the carbon cloth (Fig. 4f), due to

the contribution of both SnO_2-NSs and AC layers (Fig. S19). The mechanical strength of the CF@SnO_2-NS@AC composite is superior to that reported in the literature for any published flexible binder-free electrodes (Table S2 in the *ESI*). These results further demonstrate the excellent mechanical flexibility and the outstanding electrical and electrochemical stability of the as-prepared 3D hierarchical CF@SnO_2-NS@AC electrodes.

Motivated by the outstanding mechanical and electrical properties of the CF@SnO_2-NS@AC composite, we have investigated its electrochemical performances as a binder-free electrode (anode) for LIBs. The CV curves were recorded in a voltage range of 0.01-3V at a constant scanning rate of 0.5 mV s^{-1} (Fig. 5a). Three reduction peaks can be detected in the initial cathodic sweep. The weak cathodic peak located at 1.68 V may be assigned to the 1st cycle irreversible decomposition of SnO_2 to metallic Sn (equation 1) and the formation of the solid electrolyte interphase (SEI) according to equation 2, which disappears in the following cycles to be replaced at a lower potential of 1.22 V.[19, 90-93] The peak at 0.77 V may be attributed to the reduction reaction of Sn and Li^+ (equation 3) for lower values of *x*, and the peak at around 0.02 V can be ascribed to the continuation of the multi-step alloying process and the formation of various Li_xSn compounds at higher values of *x* (equation 3).[93-97] As described in equation 4, the participation of the CF and low crystallinity AC is also indicated especially from the cathodic peak of 0.02V.[74, 98] For large parts of the C, both the Sn and the C cathodic peaks will overlap especially for the higher values of *x* in equation 3.[53] The peak corresponding to the formation of the SEI disappears in the following cycles and the Sn multi-step alloying peak shifts toward higher potential.[99-101] Another peak appears in the cathodic scan at ~1.2 V starting from the second cycles, which may suggest that the reduction of SnO_2 is taking place at lower overpotentials offering some reversibility as shown in the anodic peak at 1.25 V.[95, 102, 103]

$$SnO_2 + 4Li^+ + 4e^- \rightarrow Sn + 2Li_2O \qquad \text{Eq. (1)}$$

$$Li^+ + e^- + \text{electrolyte} \rightarrow \text{SEI films} \quad \text{Eq. (2)}$$

$$Sn + xLi^+ + xe^- \rightarrow Li_xSn\ (0<x<4.4) \quad \text{Eq. (3)}$$

$$C + xLi^+ + xe^- \rightarrow Li_xC \quad \text{Eq. (4)}$$

The anodic scan shows almost similar behaviour for the first and the subsequent cycles. The peaks at 0.29 and 0.51 V can be assigned to the dealloying process of Li_xSn, intermetallic compounds at the lower end overlapping with any C deintercalation.[94, 95, 104, 105] The broad peak at about 1.25 V might represent the partially reversible oxidation of Sn into SnO_x.[103, 106-108] All the reduction and oxidation peaks are almost in the same position for all the subsequent cycles, revealing the excellent electrochemical reversibility of the 3D hierarchical CF@SnO_2-NS@AC electrode.

Fig. 5b presents the galvanostatic charge-discharge (GCD) curve of the flexible CF@SnO_2-NS@AC sample at a constant current density of 50 mA g^{-1}. The initial discharge and charge specific capacities are calculated to be 1253 and 1076 mAh g^{-1}, respectively. The initial Coulombic efficiency (CE) is 85.9%. The initial irreversible capacity loss may be attributed to the irreversible oxidation of lithium to form SEI film on the electrode surface.[80, 109] However, most conversion reactions in the CF@SnO_2-NS@AC structure may be more reversible than other SnO_2-based electrodes, which also can be verified by the CV (Fig. 5a) and GCD (Fig. 5b) curves. This may stem from the unique sandwich CF@SnO_2-NS@AC structure and the synergy of the outside AC layer, [95] which finally leads to a high initial CE value of 85.9%. Similar to CV results, the discharge curve has plateaus between 0.1-1 V and the charge has plateaus between 0.1-1.6 V associated with the alloying/dealloying process of Li_xSn.[110, 111] The discharge and charge capacities in the second cycle decrease to 1073 and 1066 mAh g^{-1}, respectively, which corresponds to a CE of 99.3%. The obtained capacity is higher than the theoretical capacity of SnO_2 (781 mAh g^{-1}), suggesting a possible contribution to the capacity from the CF substrate and the p partially

reversible redox reaction involving Li_2O.[101, 112] After the first cycle, both the charge and discharge curves show no visible changes, indicating the excellent reversibility of the CF@SnO_2-NS@AC electrode.

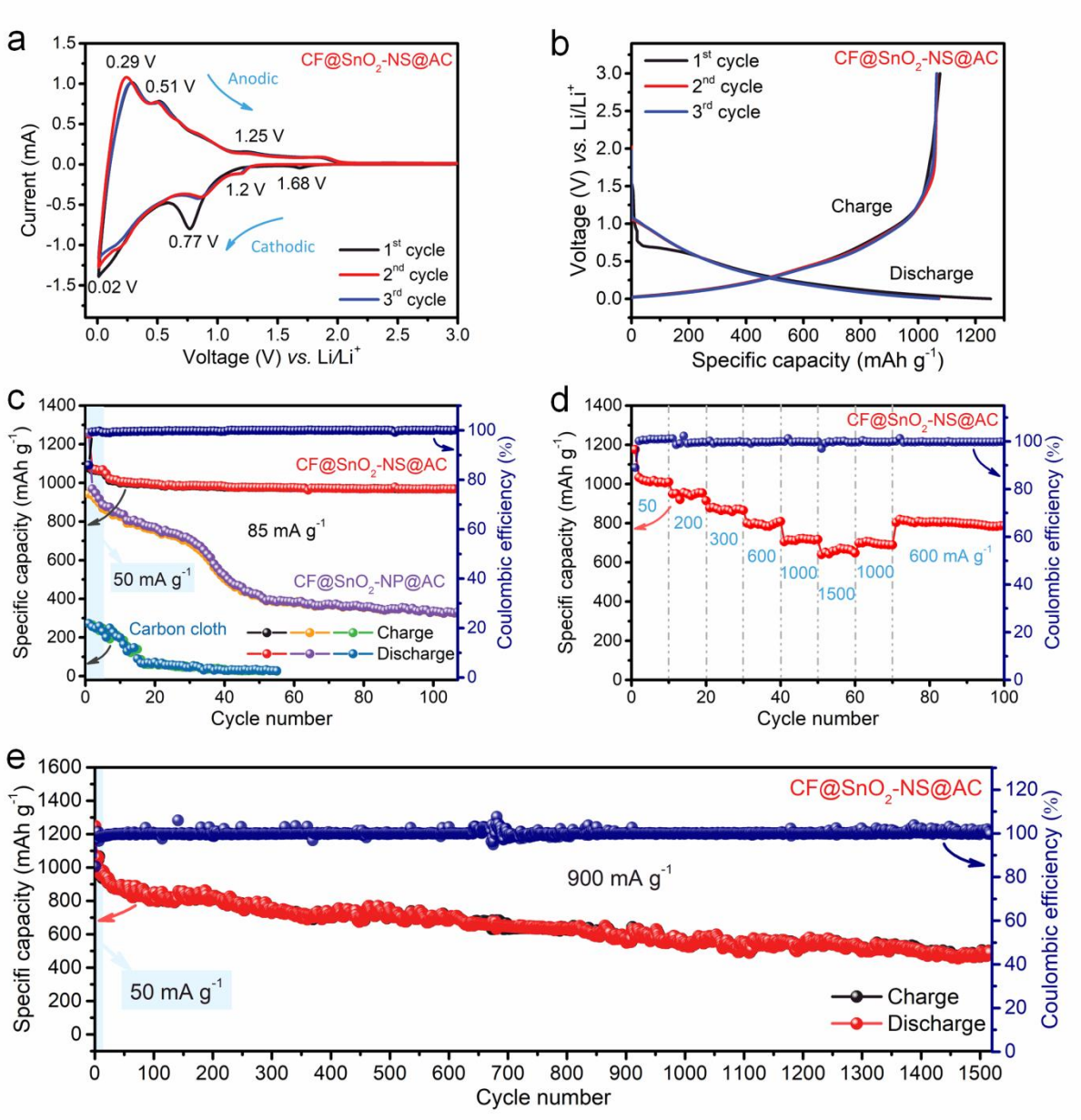

Fig. 5. Electrochemical performance of the as-prepared 3D hierarchical CF@SnO_2-NS@AC composite directly used as anode with pure Li foil: (a) CV curves at a scan rare of mV s^{-1} from 0.01 to 3 V, (b) GDC voltage profiles for the first three cycles at a current density of 50 mA g^{-1}, (c) cycling performance in comparison to CF@SnO_2-NP@AC and carbon cloth at a current density of 85 mA g^{-1} and the corresponding CE of CF@SnO_2-NS@AC, (d) rate cycle performance at different current density, (e) long-term cycling performance at 900 mA g^{-1} for 1500 cycles.

The cycling behaviour of the CF@SnO_2-NS@AC electrode was further investigated at different current densities and compared with that of the controlled sample CF@SnO_2-NP@AC. Fig. 5c presents the cycling capacities of both electrodes as well as that of the carbon cloth substrate at the current density of 85 mA g^{-1} (the current density in the first five cycles is 50 mA g^{-1} to achieve a more stable activation process). The CF@SnO_2-NS@AC electrode shows the highest specific capacity and the best cycle stability of all the tested materials. The capacity of the CF@SnO_2-NP@AC electrode dropped from 1270 mAh g^{-1} to 336 mAh g^{-1} after only 50 cycles. This significant capacity fading can be attributed to the dense structure of the electrode, which could not tolerate the volume expansion during the alloying/dealloying cycles (Fig. S20, Fig. 6a). The carbon cloth substrate displays poor cyclability, with the capacity dropping to less than 30 mAh g^{-1} after 50 cycles. In contrast, the CF@SnO_2-NS@AC electrode can still maintain high and stable discharge and charge capacities of 968.5 and 968.6 mAh g^{-1} after 100 cycles at 85 mA g^{-1}, which are about 96% capacity retention to those after the initial 10 cycles (Fig. S21). It is worthy of note that the CE of the flexible CF@SnO_2-NS@AC composites remains almost 100% after the first cycle and keeps unchanged in the following cycles, suggesting remarkable energy conversation efficiency. In comparison, the CF@SnO_2-NP@AC electrode shows a much lower CE of 74.8%, in the first cycle as presented in Fig. 5c. The rate capabilities of the CF@SnO_2-NS@AC were evaluated by recording the GCD at different current densities ranging from 50 to 1500 mA g^{-1}, as shown in Fig. 5d. Although the specific capacities decrease with the increasing current densities, the free-standing CF@SnO_2-NS@AC composite anode still presents a superior reversible capacity and prominent energy conversation efficiency. When the current densities increase to 1500 mA g^{-1}, the CF@SnO_2-NS@AC electrode can still deliver the discharge capacity of 656.2 mAh g^{-1} with a CE of about 100%. When the current density returns to 600 mA g^{-1}, the discharge capacity of as high as 820.1 mA h g^{-1} is

recovered quickly. These results reveal the outstanding rate capability of the flexible CF@SnO_2-NS@AC composites. Moreover, the flexible CF@SnO_2-NS@AC electrode also presents a good high current cycling stability (471.2 mAh g^{-1}) with almost 100% CE after 1500 cycles at 900 mA g^{-1} (Fig. 5e). Although the CF@SnO_2-NP@AC electrode exhibits a similar rate cycling performance as the CF@SnO_2-NS@AC structure (Fig. S22), its long-term cycling stability is poor. The CF@SnO2-NP@AC electrodes which could maintain a specific capacity of 235.1 mAh g^{-1} after 1000 cycles at 900 mA g^{-1} (Fig. S23). Such a high capacity, excellent cycling stability and rate capability are also not reported in the literature for SnO_2-based composites anode materials (Table S3 in the *ESI*).

The remarkable overall electrochemical performance of the CF@SnO_2-NS@AC flexible electrode can be attributed to several factors. First, the ultrathin 2D SnO_2-NSs uniformly interconnect together to form a 3D porous sponge-like structure with numerous open voids and large specific surface area, which could increase the available electrode-electrolyte contact interface, shorten the diffusion channels for Li^+ ions, and facilitate the electrolyte access to the electrode interior.[106, 113] Second, the free-standing SnO_2-NSs interlinked structure could tolerate the huge volume change arising from the repeated alloying/dealloying process.[36, 114] Third, the AC coating also provides a unique protection for maintaining the structural integrity of the electrode materials during the discharge/charge cycles, as shown in Fig. 6b. The SEM images after different cycles indicate that the 3D porous sponge-like structure could retain their original morphology covered with a gel-like SEI film (Fig. 6c-e and Fig. S24).[65] Finally, the highly conductive CF and AC layers are tightly connected with SnO_2-NSs through chemical bonds, forming an efficiently conductive network for electron and ion transport. The Nyquist curves of the electrochemical impedance spectroscopy (EIS) show that contact and charge transfer resistances of both CF@SnO_2-NS@AC and CF@SnO_2-NP@AC composites are remarkably low, due to the similar

semicircle diameter to those of conductive carbon cloth electrode in the high-frequency region (Fig. 6f, Fig. S25, and Table S4). The diameter of the semicircle in the EIS spectra of CF@SnO_2-NS@AC reduced significantly after the 5^{th} and 100^{th} cycles as shown in Fig. 6g, suggesting the reduction in the charge transfer resistance (Table S4). The improvement of the overall conductivity of the electrode after several cycles could be attributed to the enhanced inter-structure contact and improved electronic transfer between carbon and Li_xSn.[115] Furthermore, the AC coating layer can prevent the agglomeration of SnO_2-NSs and the following intermediate products, which can improve the reversibility of the lithiation/delithiation reactions.[80, 106] With synergetic interaction between the tight growth on CF substrate and meritorious protection of AC coating, the flexible CF@SnO_2-NS@AC composites could even keep the structure and electrochemical properties of electrode stable under cycles of external bending stress. Benefiting from the aforementioned advantages, the novel 3D hierarchical CF@SnO_2-NS@AC flexible architectures exhibit an enhanced reversible electrochemical performance.

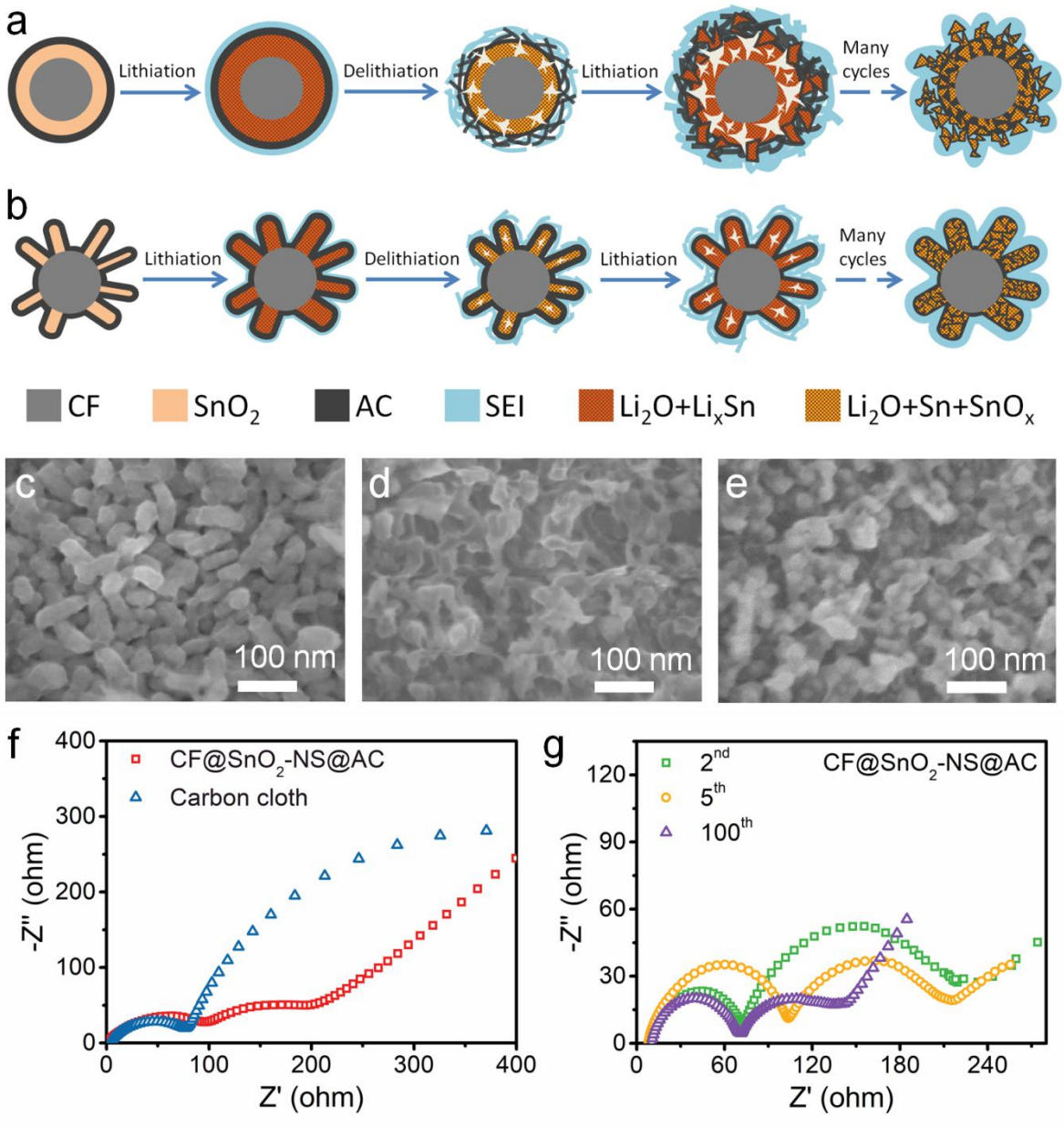

Fig. 6. Schematic illustrations for structural collapse mechanism (side cross-section view) of the electrodes CF@SnO_2-NP@AC (a) and CF@SnO_2-NS@AC (b) upon many cycles, FESEM images of the 3D hierarchical CF@SnO_2-NS@AC composite electrode after discharge/charge process for (c) 2, (d) 5, and (e) 100 cycles at 85 mA g^{-1}, (f) Nyquist plots of the carbon cloth and CF@SnO_2-NS@AC electrode at the amplitude alternating current voltage of 0.5 mV, (g) the EIS spectra of CF@SnO_2-NS@AC after various discharge/charge cycles.

Conclusion

In conclusion, we reported a novel 3D hierarchical flexible architecture by coating thin AC layer on the free-standing ultrathin SnO_2-NSs anchored on CF yarn in wearable carbon cloth substrate, via a simple hydrothermal process followed by carbon coating. The ultrathin SnO_2-NSs were vertically grown on the CF, homogenously interconnected together to form a free-standing sponge-like porous structure, and finally protected by a thin AC layer outside. The as-prepared flexible CF@SnO_2-NS@AC composite anode delivered an excellent mechanical strength and remarkable strain elongation in various directions, indicating electrochemical stability under external bending stress. After being used as a binder-free anode for LIBs, CF@SnO_2-NS@AC presented excellent electrochemical performances at room temperature. Notably, the CF@SnO_2-NS@AC electrode materials displayed a high reversible discharge specific capacity of 968.5 after 100 cycles at 85 mA g^{-1}, which is about 96% capacity retention to those after the initial 10 cycles. An extraordinary rate capability was obtained. A long cycle life with a high capacity of 471.2 mAh g^{-1} and almost 100% CE after 1500 cycles at 900 mA g^{-1} was achieved. Overall, this unique 3D hierarchical structure based on the wearable carbon cloth substrate offers such advantages as the easy approach and large contact interface with liquid electrolyte contributing to shortened path and diffusion channels of Li^+, free-standing interconnected structure for tolerating the considerable volume change, special protection for maintaining the structural integrity during discharge/charge process, tight chemical bonding between the SnO_2-NSs and the CF (or AC) layer for highly electron and ion conductive network, flexible AC cover for preventing agglomeration, as well as excellent mechanical flexibility and electrical stability for the external strain accommodation. All these could make the 3D hierarchical structure a strong candidate with significant potential prospects for high-performance flexible LIBs. This designed strategy may also inspire opportunities for preparing oxide flexible anode materials with the 3D hierarchical sandwich structure for next-generation wearable electrode devices.

Acknowledgements

This work was supported by the National Natural Science Foundation of China (No. 51702293) and the Fundamental Research Funds for the Central Universities (No. 2652017402 and 2652017342).

Supplementary information

Supporting materials associated with this article was also uploaded separately.

References

[1] Y. Wang, C. Chen, H. Xie, T. Gao, Y. Yao, G. Pastel, X. Han, Y. Li, J. Zhao, K.K. Fu, L. Hu, Advanced Functional Materials, 27 (2017) 1703140.

[2] F. Yi, H. Ren, J. Shan, X. Sun, D. Wei, Z. Liu, Chemical Society reviews, (2018).

[3] X. Cai, C. Zhang, S. Zhang, Y. Fang, D. Zou, Journal of Materials Chemistry A, 5 (2017) 2444-2459.

[4] L. Dong, G. Liang, C. Xu, W. Liu, Z.-Z. Pan, E. Zhou, F. Kang, Q.-H. Yang, Nano Energy, 34 (2017) 242-248.

[5] Y. Shao, J. Li, Y. Li, H. Wang, Q. Zhang, R.B. Kaner, Mater. Horiz., 4 (2017) 1145-1150.

[6] J. He, N. Wang, Z. Cui, H. Du, L. Fu, C. Huang, Z. Yang, X. Shen, Y. Yi, Z. Tu, Y. Li, Nature communications, 8 (2017) 1172.

[7] C. Yang, X. Ji, X. Fan, T. Gao, L. Suo, F. Wang, W. Sun, J. Chen, L. Chen, F. Han, L. Miao, K. Xu, K. Gerasopoulos, C. Wang, Advanced materials, 29 (2017).

[8] S. Hong, J. Lee, K. Do, M. Lee, J.H. Kim, S. Lee, D.-H. Kim, Advanced Functional Materials, 27 (2017) 1704353.

[9] Z. Liu, H. Li, M. Zhu, Y. Huang, Z. Tang, Z. Pei, Z. Wang, Z. Shi, J. Liu, Y. Huang, C. Zhi, Nano Energy, 44 (2018) 164-173.

[10] Y. He, B. Matthews, J. Wang, L. Song, X. Wang, G. Wu, Journal of Materials Chemistry A, 6 (2018) 735-753.

[11] G. Qian, B. Zhu, X. Liao, H. Zhai, A. Srinivasan, N.J. Fritz, Q. Cheng, M. Ning, B. Qie, Y. Li, S. Yuan, J. Zhu, X. Chen, Y. Yang, Advanced materials, (2018).

[12] M. Armand, J.-M. Tarascon, nature, 451 (2008) 652.

[13] B. Dunn, H. Kamath, J.-M. Tarascon, Science, 334 (2011) 928-935.

[14] B. Kang, G. Ceder, Nature, 458 (2009) 190.

[15] D. Larcher, J.-M. Tarascon, Nature chemistry, 7 (2015) 19.

[16] K. Amin, Q. Meng, A. Ahmad, M. Cheng, M. Zhang, L. Mao, K. Lu, Z. Wei, Advanced materials, 30 (2018).

[17] R. Wang, X. Xue, W. Lu, H. Liu, C. Lai, K. Xi, Y. Che, J. Liu, S. Guo, D. Yang, Nanoscale, 7 (2015) 12833-12838.

[18] G. Gao, S. Lu, B. Dong, W. Yan, W. Wang, T. Zhao, C.-Y. Lao, K. Xi, R.V. Kumar, S. Ding, Journal of Materials Chemistry A, 4 (2016) 10419-10424.

[19] D. Liu, Z. Kong, X. Liu, A. Fu, Y. Wang, Y.G. Guo, P. Guo, H. Li, X.S. Zhao, ACS applied materials & interfaces, 10 (2018) 2515-2525.

[20] J. Zhu, T. Wierzbicki, W. Li, Journal of Power Sources, 378 (2018) 153-168.

[21] S. Cao, X. Feng, Y. Song, X. Xue, H. Liu, M. Miao, J. Fang, L. Shi, ACS applied materials & interfaces, 7 (2015) 10695-10701.

[22] H. Lu, J. Hagberg, G. Lindbergh, A. Cornell, Nano Energy, 39 (2017) 140-150.

[23] K. Zhu, H. Gao, G. Hu, Journal of Power Sources, 375 (2018) 59-67.

[24] L. Noerochim, J.-Z. Wang, D. Wexler, Z. Chao, H.-K. Liu, Journal of Power Sources, 228 (2013) 198-205.

[25] X. Jia, Y. Kan, X. Zhu, G. Ning, Y. Lu, F. Wei, Nano Energy, 10 (2014) 344-352.

[26] S.-J. Cho, K.-H. Choi, J.-T. Yoo, J.-H. Kim, Y.-H. Lee, S.-J. Chun, S.-B. Park, D.-H. Choi, Q. Wu, S.-Y. Lee, S.-Y. Lee, Advanced Functional Materials, 25 (2015) 6029-6040.

[27] K. Xi, P.R. Kidambi, R. Chen, C. Gao, X. Peng, C. Ducati, S. Hofmann, R.V. Kumar, Nanoscale, 6 (2014) 5746-5753.

[28] K. Li, T. Zhao, H. Wang, S. Zhang, C. Deng, Journal of Materials Chemistry A, 6 (2018) 1561-1573.

[29] J. Tan, Y. Han, L. He, Y. Dong, X. Xu, D. Liu, H. Yan, Q. Yu, C. Huang, L. Mai, Journal of Materials Chemistry A, 5 (2017) 23620-23627.

[30] K. Yan, B. Sun, P. Munroe, G. Wang, Energy Storage Materials, 11 (2018) 127-133.

[31] Y.Z. Zhang, Y. Wang, T. Cheng, W.Y. Lai, H. Pang, W. Huang, Chemical Society reviews, 44 (2015) 5181-5199.

[32] X. Ma, L. Chen, X. Ren, G. Hou, L. Chen, L. Zhang, B. Liu, Q. Ai, L. Zhang, P. Si, Journal of Materials Chemistry A, (2018).

[33] C. Hwang, W.J. Song, J.G. Han, S. Bae, G. Song, N.S. Choi, S. Park, H.K. Song, Advanced materials, 30 (2018).

[34] H.G. Wang, W. Li, D.P. Liu, X.L. Feng, J. Wang, X.Y. Yang, X.B. Zhang, Y. Zhu, Y. Zhang, Advanced materials, 29 (2017).

[35] G. Wang, C. Lu, X. Zhang, B. Wan, H. Liu, M. Xia, H. Gou, G. Xin, J. Lian, Y. Zhang, Nano Energy, 36 (2017) 46-57.

[36] G. Gao, Y. Xiang, S. Lu, B. Dong, S. Chen, L. Shi, Y. Wang, H. Wu, Z. Li, A. Abdelkader, K. Xi, S. Ding, Nanoscale, 10 (2018) 921-929.

[37] L. Noerochim, J.-Z. Wang, D. Wexler, M.M. Rahman, J. Chen, H.-K. Liu, Journal of Materials Chemistry, 22 (2012) 11159.

[38] G. Zhou, F. Li, H.-M. Cheng, Energy & Environmental Science, 7 (2014) 1307-1338.

[39] Y.H. Zhu, S. Yuan, D. Bao, Y.B. Yin, H.X. Zhong, X.B. Zhang, J.M. Yan, Q. Jiang, Advanced materials, 29 (2017).

[40] Y.h. Zhu, Y.b. Yin, X. Yang, T. Sun, S. Wang, Y.s. Jiang, J.m. Yan, X.b. Zhang, Angewandte Chemie International Edition, 56 (2017) 7881-7885.

[41] B. Liu, J. Zhang, X. Wang, G. Chen, D. Chen, C. Zhou, G. Shen, Nano letters, 12 (2012) 3005-3011.

[42] V. Etacheri, J.E. Yourey, B.M. Bartlett, ACS nano, 8 (2014) 1491-1499.

[43] F.F. Cao, J.W. Deng, S. Xin, H.X. Ji, O.G. Schmidt, L.J. Wan, Y.G. Guo, Advanced materials, 23 (2011) 4415-4420.

[44] X. Xu, H. Tan, K. Xi, S. Ding, D. Yu, S. Cheng, G. Yang, X. Peng, A. Fakeeh, R.V. Kumar, Carbon, 84 (2015) 491-499.

[45] Z. Fan, J. Liang, W. Yu, S. Ding, S. Cheng, G. Yang, Y. Wang, Y. Xi, K. Xi, R.V. Kumar, Nano Energy, 16 (2015) 152-162.

[46] S. Ding, J.S. Chen, Advanced Functional Materials, 21 (2011) 4120-4125.

[47] C. Yuan, H.B. Wu, Y. Xie, X.W.D. Lou, Angewandte Chemie International Edition, 53 (2014) 1488-1504.

[48] S.-M. Paek, E. Yoo, I. Honma, Nano letters, 9 (2008) 72-75.

[49] X. Wang, X. Cao, L. Bourgeois, H. Guan, S. Chen, Y. Zhong, D.M. Tang, H. Li, T. Zhai, L. Li, Advanced Functional Materials, 22 (2012) 2682-2690.

[50] Y. Cheng, Q. Li, C. Wang, L. Sun, Z. Yi, L. Wang, Small, 13 (2017).

[51] J. Liang, W. Wei, D. Zhong, Q. Yang, L. Li, L. Guo, ACS applied materials & interfaces, 4 (2012) 454-459.

[52] X. Hou, Y. Hu, H. Jiang, Y. Li, W. Li, C. Li, Journal of Materials Chemistry A, 3 (2015) 9982-9988.

[53] L. Xia, S. Wang, G. Liu, L. Ding, D. Li, H. Wang, S. Qiao, Small, 12 (2016) 853-859.

[54] J. Fan, T. Wang, C. Yu, B. Tu, Z. Jiang, D. Zhao, Advanced materials, 16 (2004) 1432-1436.

[55] J.S. Chen, X.W.D. Lou, Small, 9 (2013) 1877-1893.

[56] J.-I. Lee, J. Song, Y. Cha, S. Fu, C. Zhu, X. Li, Y. Lin, M.-K. Song, Nano Research, 10 (2017) 4398-4414.

[57] Z. Chen, J.W.F. To, C. Wang, Z. Lu, N. Liu, A. Chortos, L. Pan, F. Wei, Y. Cui, Z. Bao, Advanced Energy Materials, 4 (2014) 1400207.

[58] X. Dong, L. Chen, X. Su, Y. Wang, Y. Xia, Angewandte Chemie, 55 (2016) 7474-7477.

[59] V. Etacheri, G.A. Seisenbaeva, J. Caruthers, G. Daniel, J.-M. Nedelec, V.G. Kessler, V.G. Pol, Advanced Energy Materials, 5 (2015) 1401289.

[60] R. Huang, L. Wang, Q. Zhang, Z. Chen, Z. Li, D. Pan, B. Zhao, M. Wu, C.M. Wu, C.H. Shek, ACS nano, 9 (2015) 11351-11361.

[61] S.H. Lee, W.B. Kim, Journal of Power Sources, 307 (2016) 38-44.

[62] S.H. Lee, Y.-R. Jo, Y. Noh, B.-J. Kim, W.B. Kim, Journal of Power Sources, 367 (2017) 1-7.

[63] M. Wang, L. Fan, X. Wu, D. Tian, J. Cheng, Y. Qiu, H. Wu, B. Guan, N. Zhang, K. Sun, Y. Wang, Journal of Materials Chemistry A, 5 (2017) 19613-19618.

[64] Y. Zhang, Q. Xiao, G. Lei, Z. Li, X. Li, Electrochimica Acta, 178 (2015) 336-343.

[65] L. Liu, F. Xie, J. Lyu, T. Zhao, T. Li, B.G. Choi, Journal of Power Sources, 321 (2016) 11-35.

[66] J.Y. Cheong, J.H. Chang, H.K. Seo, J.M. Yuk, J.W. Shin, J.Y. Lee, I.-D. Kim, Nano Energy, 25 (2016) 154-160.

[67] G.D. Park, J.-K. Lee, Y.C. Kang, Advanced Functional Materials, 27 (2017) 1603399.

[68] H. Bian, Y. Tian, C. Lee, M.F. Yuen, W. Zhang, Y.Y. Li, ACS applied materials & interfaces, 8 (2016) 28862-28871.

[69] X. Hu, G. Zeng, J. Chen, C. Lu, Z. Wen, Journal of Materials Chemistry A, 5 (2017) 4535-4542.

[70] H. Bian, R. Dong, Q. Shao, S. Wang, M.-F. Yuen, Z. Zhang, D.Y.W. Yu, W. Zhang, J. Lu, Y.Y. Li, Journal of Materials Chemistry A, 5 (2017) 23967-23975.

[71] G.D. Park, Y.C. Kang, Nano Research, 11 (2018) 1301-1312.

[72] M. Li, Q. Deng, J. Wang, K. Jiang, Z. Hu, J. Chu, Nanoscale, 10 (2018) 741-751.

[73] F. Zhang, C. Yang, X. Gao, S. Chen, Y. Hu, H. Guan, Y. Ma, J. Zhang, H. Zhou, L. Qi, ACS applied materials & interfaces, 9 (2017) 9620-9629.

[74] Y. Cheng, Q. Li, C. Wang, L. Sun, Z. Yi, L. Wang, Small, 13 (2017).

[75] F. Zhang, L. Qi, Advanced science, 3 (2016) 1600049.

[76] H. Xie, M. Chen, L. Wu, Small, 13 (2017).

[77] G.H. An, D.Y. Lee, Y.J. Lee, H.J. Ahn, ACS applied materials & interfaces, 8 (2016) 30264-30270.

[78] Y. Zeng, J. Luo, Y. Wang, L. Qiao, B. Zou, W. Zheng, Nanoscale, 9 (2017) 17576-17584.

[79] J. Cui, S. Yao, J.-Q. Huang, L. Qin, W.G. Chong, Z. Sadighi, J. Huang, Z. Wang, J.-K. Kim, Energy Storage Materials, 9 (2017) 85-95.

[80] J. Qin, N. Zhao, C. Shi, E. Liu, F. He, L. Ma, Q. Li, J. Li, C. He, Journal of Materials Chemistry A, 5 (2017) 10946-10956.

[81] L. Wang, J. Yan, Z. Xu, W. Wang, J. Wen, X. Bai, Nano Energy, 42 (2017) 294-299.

[82] A.C. Ferrari, Solid State Communications, 143 (2007) 47-57.

[83] A.C. Ferrari, D.M. Basko, Nature nanotechnology, 8 (2013) 235.

[84] A.C. Ferrari, J.C. Meyer, V. Scardaci, C. Casiraghi, M. Lazzeri, F. Mauri, S. Piscanec, D. Jiang, K.S. Novoselov, S. Roth, A.K. Geim, Physical review letters, 97 (2006) 187401.

[85] A.C. Ferrari, J. Robertson, Physical review B, 61 (2000) 14095.

[86] C. Casiraghi, A.C. Ferrari, J. Robertson, Physical Review B, 72 (2005).

[87] A.C. Ferrari, J. Robertson, Philosophical transactions. Series A, Mathematical, physical, and engineering sciences, 362 (2004) 2477-2512.

[88] A.C. Ferrari, J. Robertson, Physical Review B, 64 (2001).

[89] H. Hu, H. Cheng, G. Li, J. Liu, Y. Yu, Journal of Materials Chemistry A, 3 (2015) 2748-2755.

[90] M. Zhang, Z. Sun, T. Zhang, D. Sui, Y. Ma, Y. Chen, Carbon, 102 (2016) 32-38.

[91] Y. Jiang, Y. Li, P. Zhou, S. Yu, W. Sun, S. Dou, ACS applied materials & interfaces, 7 (2015) 26367-26373.

[92] M. Zhou, Y. Liu, J. Chen, X. Yang, Journal of Materials Chemistry A, 3 (2015) 1068-1076.

[93] L.P. Wang, Y. Leconte, Z. Feng, C. Wei, Y. Zhao, Q. Ma, W. Xu, S. Bourrioux, P. Azais, M. Srinivasan, Z.J. Xu, Advanced materials, 29 (2017).

[94] J. Lin, Z. Peng, C. Xiang, G. Ruan, Z. Yan, D. Natelson, J.M. Tour, ACS nano, 7 (2013) 6001-6006.

[95] R. Hu, Y. Ouyang, T. Liang, H. Wang, J. Liu, J. Chen, C. Yang, L. Yang, M. Zhu, Advanced materials, 29 (2017).

[96] Y. Tan, K.W. Wong, K.M. Ng, Small, 13 (2017).

[97] H. Kim, G.O. Park, Y. Kim, S. Muhammad, J. Yoo, M. Balasubramanian, Y.-H. Cho, M.-G. Kim, B. Lee, K. Kang, H. Kim, J.M. Kim, W.-S. Yoon, Chemistry of Materials, 26 (2014) 6361-6370.

[98] K. Lee, S. Shin, T. Degen, W. Lee, Y.S. Yoon, Nano Energy, 32 (2017) 397-407.

[99] X. Zhou, L. Yu, X.W.D. Lou, Advanced Energy Materials, 6 (2016) 1600451.

[100] R. Hu, D. Chen, G. Waller, Y. Ouyang, Y. Chen, B. Zhao, B. Rainwater, C. Yang, M. Zhu, M. Liu, Energy & Environmental Science, 9 (2016) 595-603.

[101] B. Huang, X. Li, Y. Pei, S. Li, X. Cao, R.C. Masse, G. Cao, Small, 12 (2016) 1945-1955.

[102] X. Wang, L. Zhang, C. Zhang, P. Wu, Inorganic Chemistry Frontiers, 4 (2017) 889-897.

[103] L. Yang, T. Dai, Y. Wang, D. Xie, R.L. Narayan, J. Li, X. Ning, Nano Energy, 30 (2016) 885-891.

[104] Chemistry a European Journal.

[105] Y. Li, H. Zhang, P. Kang Shen, Nano Energy, 13 (2015) 563-572.

[106] Y. Wang, Z. Jiao, M. Wu, K. Zheng, H. Zhang, J. Zou, C. Yu, H. Zhang, Nano Research, 10 (2017) 2966-2976.

[107] D. Pan, N. Wan, Y. Ren, W. Zhang, X. Lu, Y. Wang, Y.S. Hu, Y. Bai, ACS applied materials & interfaces, 9 (2017) 9747-9755.

[108] D. Kang, Q. Liu, M. Chen, J. Gu, D. Zhang, ACS nano, 10 (2016) 889-898.

[109] X. Ao, J. Jiang, Y. Ruan, Z. Li, Y. Zhang, J. Sun, C. Wang, Journal of Power Sources, 359 (2017) 340-348.

[110] Y. Zhao, L.P. Wang, S. Xi, Y. Du, Q. Yao, L. Guan, Z.J. Xu, Journal of Materials Chemistry A, 5 (2017) 25609-25617.

[111] Y. Cheng, J. Huang, H. Qi, L. Cao, X. Luo, J. Li, Z. Xu, J. Yang, Nanoscale, 9 (2017) 18681-18689.

[112] H. Wang, J. Wang, D. Cao, H. Gu, B. Li, X. Lu, X. Han, A.L. Rogach, C. Niu, Journal of Materials Chemistry A, 5 (2017) 6817-6824.

[113] Y. Zhang, Z. Hu, Y. Liang, Y. Yang, N. An, Z. Li, H. Wu, Journal of Materials Chemistry A, 3 (2015) 15057-15067.

[114] Z. Wang, J. Sha, E. Liu, C. He, C. Shi, J. Li, N. Zhao, Journal of Materials Chemistry A, 2 (2014) 8893-8901.

[115] S. Prabakar, Y.H. Hwang, E.G. Bae, S. Shim, D. Kim, M.S. Lah, K.S. Sohn, M. Pyo, Advanced materials, 25 (2013) 3307-3312.